nature sustainability

Article

https://doi.org/10.1038/s41893-026-01780-4

Biodegradable yet hyperdurable robotic fingers for zero-waste soft electronics

Received: 8 April 2025

Accepted: 28 January 2026

Kyung-Sub Kim[1,2,17], Jun-Seok Shim[1,17], Sung-Woo Kim[1,17], Gyeong-Seok Hwang[3], You-Jung Park[1], Joran Booth[4], Jae-Young Bae[1,2], Jong-hyoung Kim[5], Min-Ha Oh[1], Minseong Chae[1,6], Jooik Jeon[7], Ju-Yong Lee[1], Jae-Hwan Lee[1,8], Min-Jung Chae[1,9], Sung-Geun Choi[1,9], Young-Seo Kim[1], Seung-Min Lee[1], Se-Hun Kang[1], Joo-Hyeon Park[1], Yong-Wu Kim[1], Woo-Jin Lee[1], Im-Deok Kim[1], Ki-Hyun Kim[1], Seong-Yu Choi[1], Jeong-Yun Sun[1,2], Rebecca Kramer-Bottiglio[4], Myoung-Ryul Ok[9,10], Jae Joon Kim[11], Jung Keun Hyun[12], Kang-Sik Lee[6], Ju-Young Kim[3], Sang Yup Kim[4,13] ✉, Martin Kaltenbrunner[14,15] ✉ & Seung-Kyun Kang[1,2,8,16] ✉

Adopting compostable materials that return to nature akin to organisms can mitigate concerns regarding the ecological footprint associated with the widespread deployment of soft robots across various fields, including medicine, agriculture and environmental exploration. Nevertheless, current implementations are constrained by the lack of reliability of sustainable soft actuators, difficulties in achieving multifunctionality of biodegradable electronics, and uncertain eco-compatibility of by-products. Here we address these challenges by providing a framework that integrates sophisticated transient inorganic electronics with durable yet degradable elastomer (polyglycerol sebacate) and polyanhydride-based adhesive in compostable soft embodiments. Our soft electronic fingers withstand over 1,000,000 actuation cycles and feature 21 high-density electronic components that enable proprio-/exteroceptive sensing and environmental intervention. The high survival rates of oats germinated in soils containing feedstock composted from not only polymers but also electronic materials, such as Si, Mo and Mg, indicate that our robot is seamlessly integrated into the ecosystem. All these advances bridge the gap between sustainability and performance in soft robots.

Driven by recent progress in the robotics industry, robot adoption rates have surged and more than doubled over the past decade, according to the World Robotics 2025 report from the International Federation of Robotics. However, this rapid growth also raises the risk that end-of-life robots may become a major source of industrial pollution. This concern is further compounded by the rise in electronic waste, which is projected to grow by ~2 megatons annually, starting at 56.3 megatons in 2019[1]. These converging trends indicate that future soft robots, which rely on soft electronics for adaptability and complex functionality, will inevitably exacerbate waste management challenges. In particular, the widespread use of cross-linked resins and composite materials, combined with miniaturized, high-resolution, multilayer thin-film structures, complicates recycling and repair in next-generation soft robotic systems. In this context, adopting biodegradable materials to achieve a zero-waste strategy is emerging as a critical breakthrough for sustainable robotic systems[1–13].

Biodegradable soft robots aim to mimic living organisms[1–13] not only during life through diverse functionality and adaptability but also

A full list of affiliations appears at the end of the paper. ✉e-mail: sangyupkim@sogang.ac.kr; m.w.kaltenbrunner@jku.at; kskg7227@snu.ac.kr

Fig. 1 | Components and functionality of a fully compostable multiperceptive soft robot. a, Conceptual illustration demonstrating the versatility of fully compostable advanced soft robots. **b**, Fully compostable soft robotic finger comprising a proprioceptive bendable actuator finger body and an exteroceptive electronic fingertip with multifunctionality. A PLA connector connects the finger to the pneumatic line and protect the connection (top left). The PGS-framed bending actuator consists of a PBAT strain limiter, a sensor-integrated PGS frame and PBTPA adhesive (middle left). The fingertip comprises an electronics-integrated PBAT substrate and a PBTPA block (bottom left). A Mg curvature sensor and Mo/PBAT strain sensors are attached to the surface of the PGS frame (top right). A Si temperature sensor, a Si pH sensor, Mo tactile sensors, a Mg humidity sensor, a Mg electrical stimulator, a Mg heater and a Mg/gelatin drug-releasing device are integrated onto the PBAT substrate (bottom right).

after death through eco-friendly carbon and nutrient cycling. Their promising potential applications span a range of environmentally sensitive fields, including medicine[5,14], environmental exploration[4,5,13,15] and agriculture[16]. Among living beings, humans represent a particularly aspirational model not only in terms of advanced, intelligent behaviour but also as a biological system that, in principle, adheres to a sustainable cycle with enduring functionality over a lifetime, eventual biodegradation and reintegration into the ecosystem. To emulate such characteristics, biodegradable robots must be designed with: (1) excellent storage stability and mechanical durability, (2) dense integration of miniaturized, multifunctional sensors, and (3) complete compostability such that their remnants serve as feedstock for new life.

However, achieving reliable functionality remains a formidable challenge, owing to the intrinsic limitations of biodegradable materials. For instance, hydrogels such as gelatin[1,6–8], polyvinyl alcohol (PVA)[9], chitosan[10] and cellulose[10] exhibit more rapid decline in performance after fabrication compared with water-free polymers. Elastomeric polyesters could be a promising solution, but among them, poly (L-lactide-co-ε-caprolactone) (PLCL)[11] exhibits considerable hysteresis and softening compared to elastomers such as silicone, which may hinder long-term actuation. Moreover, previous biodegradable robots equipped with tactile[6,11], curvature[7], proximity[7] and temperature[11] sensors often provide only single-function perception, and some employ sensors that are only partially degradable[6,12]. Although compostability has been reported in certain systems[1,8,11,12], these examples largely exclude electronic components and fail to demonstrate whether degradation by-products can serve as nutrient sources for new organisms, such as plants.

Here we present fully compostable soft robotic systems that seamlessly unify mechanical robustness, intelligent functionality and ecological sustainability. Our system combines long-lasting soft actuators, engineered from a water-free polyglycerol sebacate (PGS) elastomer exhibiting low hysteresis and exceptional cyclic durability, with versatile, biodegradable electronics capable of multimodal sensing and control (Fig. 1a). This integration enables the robots to perform adaptive, continuous tasks in complex environments while maintaining material integrity throughout their operational lifetime. Crucially, despite their high level of functional and structural sophistication, all components of the system including sensors, circuits and actuators undergo complete decomposition under industrial composting conditions. The resulting by-products are not only environmentally benign, but also serve as nutrient-rich feedstock capable of supporting new plant growth by enhancing enzyme activation, improving stress resistance and stimulating soil microbial activity. By achieving both reliable performance and full reintegration into the ecological cycle, our work offers a tangible model for truly sustainable robotics, where advanced machines can live, function and return to nature much like the organisms they are designed to emulate.

We selected a soft robotic finger as an example of an intricate robotic system that effectively demonstrates the capability for fine sensing during the interaction involved in the actuation motion, as well as the precise control based on it. The soft robotic finger comprises a finger base, a pneumatic PGS-framed bending actuator and a multifunctional fingertip (Fig. 1b, left). The finger base consists of a polylactic acid (PLA) connector and a cover that secure the top of the actuator together with a polybutylene adipate terephthalate (PBAT) cable. In the actuator, a polybutanedithiol–1,3,5-triallyl-1,3,5-triazine-2,4,6(1H,3H,5H)-trione pentenoic anhydride (PBTPA) adhesive with sufficient level of flexibility and low toxicity seals the cylindrical PGS frame and anchors a PBAT strain limiter, ensuring the desired bending motion. A Mg capacitive curvature sensor and Mo/PBAT resistive strain sensors, interconnected through serpentine Mg electrodes (Fig. 1b, top right), are integrated on the actuator surface. The fingertip consists of a PBTPA block and a PBAT substrate supporting a variety of electronic components, including a silicon nanomembrane (Si NM) diode temperature sensor, a Si nanoribbon pH sensor, an array of Mo-based crack tactile sensors, a Mg capacitive humidity sensor, a Mg pad for electrical stimulation, a Mg Joule heater and a Mg/gelatin thermo-responsive drug release device (Fig. 1b, bottom right). The inorganics used all possess high electrical conductivity, biodegradability and flexibility, ensuring sustainable and reliable electronic performance.

Results

PGS as reliable and electronics-compatible robotic frames

PGS exhibits excellent stretchability and elasticity, enduring high uniaxial strains without breaking, and returning perfectly to its original state while also remaining undamaged under various deformations such as biaxial stretching, folding, twisting and poking (Fig. 2a,b and Supplementary Video 1). The mechanical properties of PGS depend on the curing time; we used PGS cured for 14 h with pre-polymer for robot fabrication (Methods, Supplementary Notes and Supplementary Fig. 1). Our PGS exhibited an elastic strain range of ~345%, an elastic modulus of ~12 kPa, an ultimate tensile strength of ~26 kPa and a toughness of ~76 kJ m^{-3} (Supplementary Fig. 1) while showing low hysteresis loss ratios of less than ~11.3% during loading–unloading tensile tests (Fig. 2b and Supplementary Fig. 2a). In particular, cyclic loading–unloading tensile tests at a uniaxial strain of 100% exhibited negligible hysteresis (hysteresis loss ratios < ~11.4%) and a softening effect (cyclic stress softening ratios <~14%) for up to 10,000 cycles (Fig. 2c and Supplementary Fig. 2b,c). Our PGS thus stands out as an elastomer with the lowest hysteresis and high durability compared with other biodegradable elastomeric polyesters, including PLCL[11,17], poly(1,8-octanediol-co-citric acid) (POC)[18,19] and bio-polyurethane (bio-PU)[20–22] (Supplementary Notes, Supplementary Figs. 3 and 4 and Supplementary Table 1). The low hysteresis of PGS is probably attributed to the relatively short chain length between crosslinks (Supplementary Notes). In addition, the low production cost of PGS[23] is suitable for disposable concepts of biodegradable soft robots employed in various industrial fields (Supplementary Table 2). Equally important, Fig. 2d and Supplementary Fig. 5 demonstrate that PGS stored in an ambient environment for up to ~1.4 years (510 days) showed no considerable age-related changes, at least when kept under an ambient environment at room temperature and 60–75% relative humidity. A slight increasing trend in the elastic modulus is attributable to slow post curing in ambient condition (Supplementary Notes).

The resilient and durable nature of PGS ensures excellent reliability of PGS-framed bending actuators. Here we bond a PGS elastomer layer with PBAT strain limiters and roll them into a cylindrical actuator using PBTPA adhesive (Supplementary Figs. 6 and 7). We tested bending angles ranging from 0° to ~50° during cyclic actuation, finding that both the pressure-dependent bending angle and blocking force for as-fabricated and 6-month-stored actuators exhibited very small hysteresis with no considerable changes after 1,000,000 actuation cycles (Fig. 2e,f). Figure 2g indicates that the actuator consistently produced a maximum blocking force (when P_{in} = 10.6 kPa) of ~1 N over 1,000,000 actuation cycles, demonstrating improved durability compared with previously reported biodegradable and resilient actuators (~0.2 N, 330,000 cycles)[5]. The bending angles at maximum applied pressure for the as-fabricated and 6-month-stored actuators were 50.1° and 50.4° in the 1st cycle, and 53.0° and 54.0° in the 1,000,000th cycle, respectively (Fig. 2h,i and Supplementary Video 2). With increasing actuation speed, the bending angle shows an increasing tendency to lag behind the rapid pressure fluctuations, whereas a distinct hysteresis between the inflation and deflation curves is not evident (Supplementary Fig. 8 and Supplementary Video 2). The sufficient levels of durability and storage stability of PBTPA and PBAT, along with the adhesion properties of PBTPA, substantially contribute to the excellent reliability of the PGS-framed bending actuators (Supplementary Notes, Supplementary Figs. 9–12 and Supplementary Video 3). Failure occurred when the bending angle of the actuator exceeded ~100° (P_{in} = 14.6 kPa) (Supplementary Fig. 13 and Supplementary Video 4).

Beyond their excellent mechanical properties, we aim at biodegradable soft materials that are inherently compatible with transient electronics. Here, water-based hydrogels are a limitation, while water-free PGS allows for durable integration, as demonstrated by serial images, resistance and thickness changes of Mg electrodes on PGS elastomer and gelatin hydrogel substrates (Fig. 2j–l). Mg electrodes on PGS showed lifespan stability of up to 6 months, with the adhesion force between Mg and PGS remaining nearly unchanged (Supplementary Fig. 14). By contrast, Mg electrodes on gelatin hydrogel dissolved within 2 days.

Multiperception and multifunctionality of robotic finger

Going beyond reliable actuation, we now integrate electronic sheets with the bending actuator to arrive at a sophisticated soft robotic finger (fabrication details in Supplementary Fig. 15). These electronic devices were produced in sheet form using sophisticated two-dimensional (2D) processes, including laser cutting[24], metal deposition[25–28], photolithography[25] and transfer printing[25–28], enabling batch production of high-resolution sensor arrays and interconnection electrodes. Detailed fabrication procedures and geometries are provided in Methods and Supplementary Figs. 15–21. Although certain microfabrication processes may raise sustainability concerns from the use of hazardous solvents, these solvents can be reclaimed using industrial recovery technologies, and the future application of such technologies in manufacturing could help ensure high sustainability of the overall system and production process. Figure 3a–f illustrates the performance of the sensors and treating electronics integrated into the soft robotic fingers. The capacitance of the Mg curvature sensor changed from ~14.99 to ~13.99 pF as the bending angle increased from 0° to ~52.5° (Fig. 3a). The resistance change ($\Delta R/R_0$) of all the Mo/PBAT resistive strain sensors (SA (sensors for axial expansion) 1–4 and SR (sensors for radial expansion) 1–4) increased up to ~4.96 when subjected to uniaxial strain of up to 80% (Fig. 3b). The strain sensors were designed for selective strain detection along a single axis (Supplementary Fig. 22). The resistance change ($\Delta R/R_0$) of all the Mo crack-based tactile sensors (Tac1–6) arranged in a 2 × 3 array at the fingertip increased up to ~1.64 when

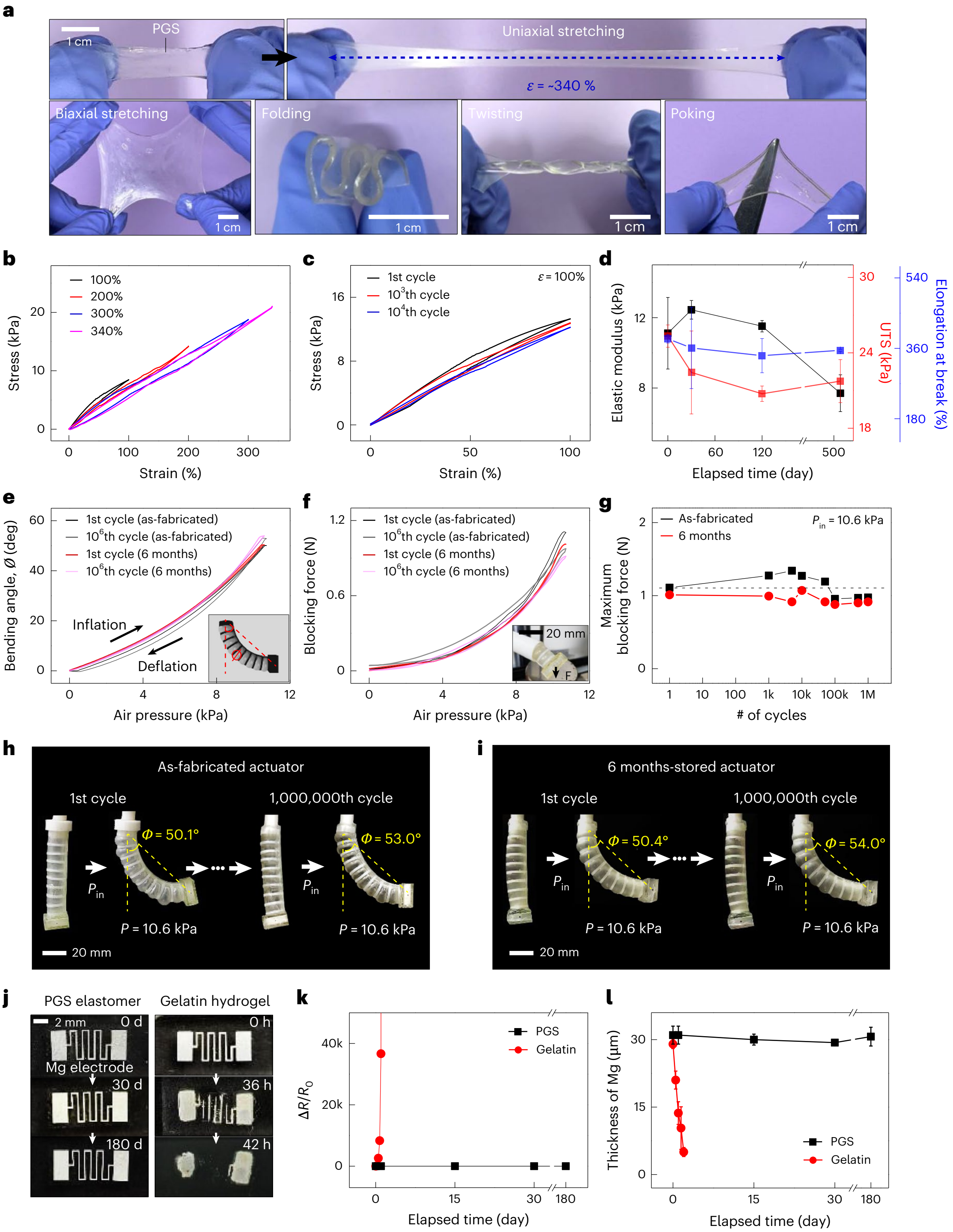

Fig. 2 | Reliable PGS elastomer and PGS-framed bending actuator. **a**, Elastic response of the PGS elastomer (1 mm thick, 40 × 10 mm) with a linear strain of ~340% (top). PGS elastomers under various deformation modes: biaxial stretching (bottom far left), folding (bottom left), twisting (bottom right) and poking (bottom far right). **b**, Loading–unloading curves of PGS under uniaxial tensile strain ranging from 100% to 340%, showing low hysteresis. **c**, Cyclic mechanical behaviours of PGS under uniaxial tensile strain of 100% over 10,000 cycles, indicating high durability. **d**, Changes in the elastic modulus (E), ultimate tensile strength (UTS, σ_b) and elongation at break (ε_b) of PGS over a storage period of 510 days in ambient environment, showing high storage stability. **e**,**f**, Bending angle (**e**) and blocking force (**f**) responding to applied pressures ranging from 0 to 10.6 kPa during the first and millionth actuations of both the as-fabricated actuator and the actuator stored for 6 months. The inset in **f** shows the setup for measuring the blocking force of the actuator. **g**, Maximum blocking force of the as-fabricated actuator and the actuator stored for 6 months at an internal pressure of 10.6 kPa. **h**,**i**, Inflation trajectories during the first and millionth actuations of the as-fabricated PGS actuator (**h**) and the actuator stored for 6 months (**i**). Internal air pressure rises from 0 to 10.6 kPa, then descends to 0 kPa during each cycle. **j**–**l**, The excellent compatibility of PGS for water-soluble electronics integration, demonstrated by serial images (**j**), resistance change (**k**) and thickness change (**l**) of Mg electrodes (~30 μm thick) integrated onto PGS and gelatin hydrogel substrates. **d**,**l**, Data are presented as mean ± s.d. of $n = 3$ independent measurements.

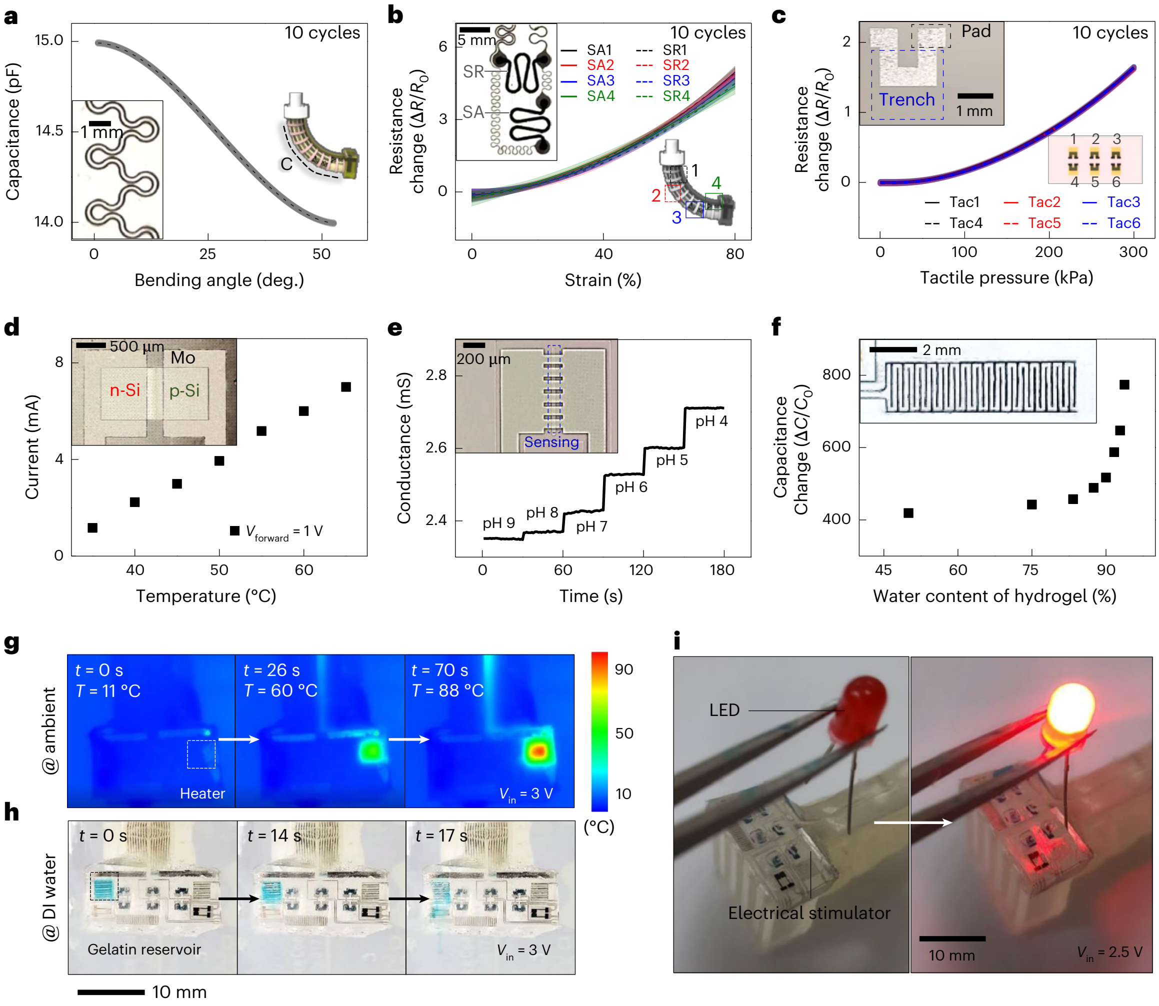

Fig. 3 | Biodegradable electronics integrated into the soft robotic finger for multiperception and multifunctionality. a,**b**, Calibration curves of the Mg curvature sensor (**a**) and the 8 Mg local strain sensors (**b**) (SA1–4, SR1–4) detecting strain in two directions (solid, axial; dashed, radial) at various positions (black, top; red, upper middle; blue, lower middle; green, bottom). **c**, Calibration curves of the 6 Mo crack-based tactile sensors (Tac 1–6) arranged in two rows (solid, 1st row; dashed, 2nd row) and three columns (black, 1st column; red, 2nd column; blue, 3rd column). **d**–**f**, Calibration curves of the Si nanomembrane PIN diode-based temperature sensor (**d**), p-doped Si nanoribbon-based pH sensor (**e**) and Mg humidity sensor (**f**). **g**,**h**, Serial images of heating in an ambient environment using the heater alone (**g**) and drug release in deionized (DI) water using the heater and a thermo-responsive gelatin reservoir containing blue ink (**h**). **i**, Demonstration of lighting an LED upon contact with an electrical stimulator applying 2.5 V. **a**,**b**, Solid and dashed lines show polynomial fits to 10 consecutive cycles of each curvature and local strain sensor component. **c**, Solid and dashed lines show fits of 10 consecutive cycles of each tactile sensor component using the theoretical model from Supplementary Fig. 30c. Shaded areas around all calibration curves indicate 95% confidence intervals over the 10 cycles.

subjected to tactile pressure of up to 300 kPa[29] (Fig. 3c). The tactile sensors included PBTPA bumps that focused stress during the application of external forces, enhancing their sensitivity (Supplementary Notes and Supplementary Fig. 17). Finite element analysis (FEA) results showed that the amplified strain from the bumps did not damage the surrounding brittle thin-film electronics (Supplementary Notes and Supplementary Figs. 23 and 24). The sensitivity of the tactile sensor was tunable (Supplementary Notes), and the highly sensitive tactile sensor array achieved a minimum detectable tactile pressure of 0.2 kPa, enabling the detection of extremely small forces (Supplementary Fig. 25). The curvature, strain and tactile sensors exhibited almost identical calibration curves after being stored at room temperature for 4 months, and they worked reliably without failure during 2,000 cycles of deformation (Supplementary Notes and Supplementary Figs. 26 and 27). The Si diode temperature sensor showed a sensitivity of −7.86 mV °C^{-1} under a current of 0.1 mA (Fig. 3d). The conductance of the p-doped Si nanoribbon pH sensor increased with decreasing pH due to charge carrier accumulation[26] (Fig. 3e). The capacitance of the Mg humidity sensor increased with increasing water content of an adjacent hydrogel due to dielectric constant changes depending on hydration levels[6,30] (Fig. 3f).

The integration of treating electronics not only provides sensing capabilities but also enables more diverse responses, including active intervention. Figure 3g–i, Supplementary Fig. 28 and Supplementary Videos 5–7 illustrate the performance of representative devices, including a Mg Joule heater, a thermo-responsive drug release device and a Mg electrical stimulator. These devices potentially enable various tasks in manufacturing, agriculture, medicine and environmental exploration, such as heat therapy[31], emergency haemostasis[32], disinfection[33], water purification[34], electrotherapy[35] and pest control[36]. Detailed descriptions of the I/O interface interconnecting the numerous electronics with the aligned Mg lines can be found in Supplementary Notes and Supplementary Figs. 16 and 20.

Figure 4, Supplementary Fig. 29 and Supplementary Videos 8 and 9 demonstrate the real-time operation of all integrated electronics, simultaneously detecting and chemically/physically modulating interactions between the soft robotic finger and external unknown objects.

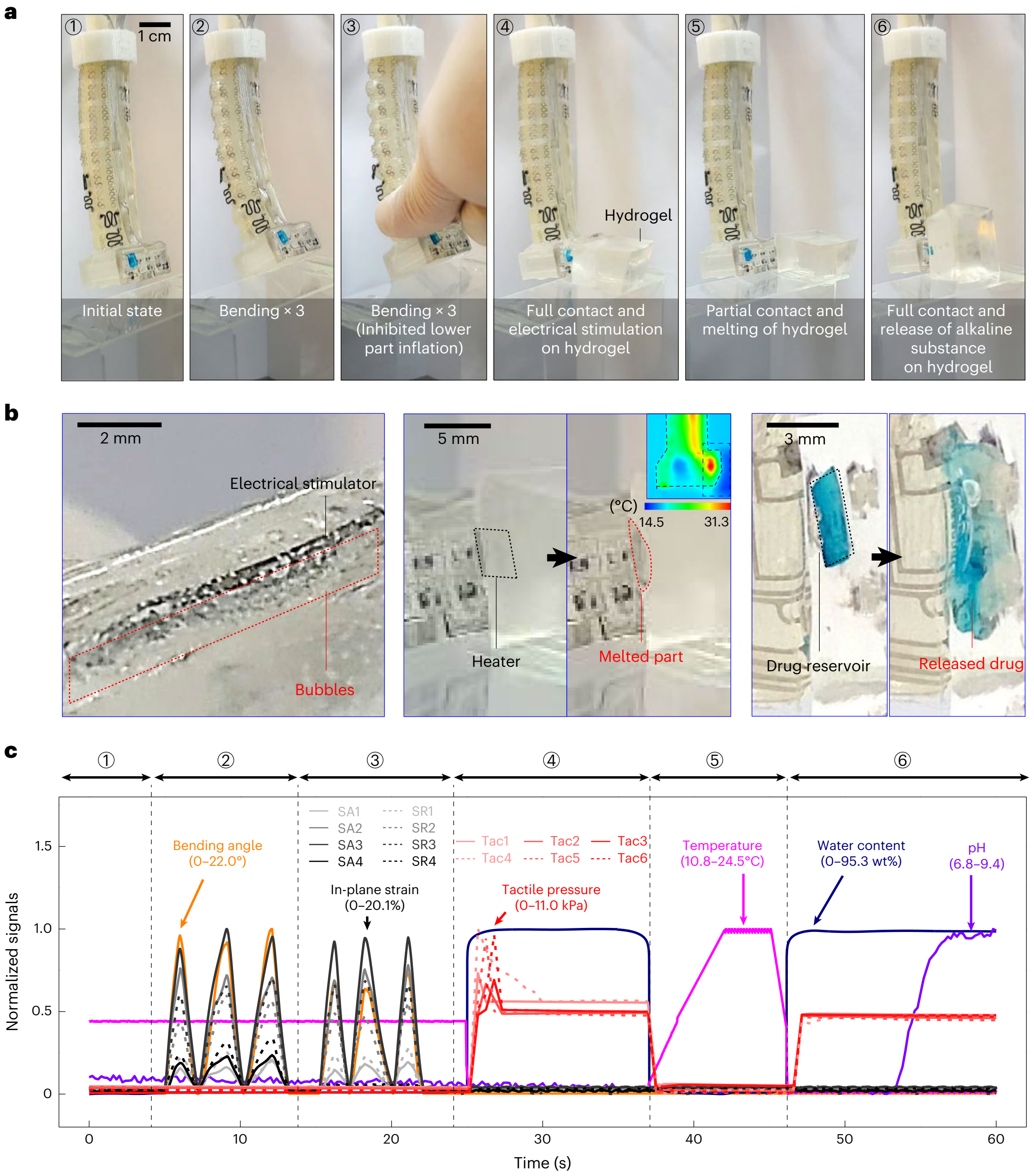

Fig. 4 | Real-time operation of the soft robotic fingers and all integrated electronics. a, Serial images during a demonstration including 6 steps: step 1, initial state; step 2, three cyclic bending motions; step 3, three cyclic bending motions with partial restriction of deformation; step 4, full contact on hydrogel and electrical stimulation; step 5, partial contact on hydrogel and heating; step 6, full contact on hydrogel and drug release with reservoir containing blue ink and NaOH solution. **b**, Bubble formation from the electrical stimulator in step 4 (left), gelatin melting induced by the heater in step 5 (middle) and drug release from the reservoir in step 6 (right). **c**, Real-time data feedback during a demonstration including the 6 steps.

This demonstration consists of 6 steps, as depicted in the series of images (Fig. 4a,b) and the normalized data feedback (Fig. 4c). All data were processed using the calibration curves in Supplementary Fig. 30. In step 3, the lack of response from the deformation-restricted SA4 and SR4 strain sensors highlights the ability to monitor the strain distribution of the robot in real time. In steps 4–6, simultaneous responses from the tactile, temperature, humidity and pH sensors were observed during interactions between the fingertip and the hydrogel, including contact, electrical stimulation, heating and drug release. Detailed descriptions of the sensor responses are provided in Supplementary Notes. These demonstrations emphasize the potential of robotic and electronic systems working seamlessly together in a synchronized manner.

Environmental interaction of robotic gripper

Agricultural settings represent an unstructured, dynamic environment particularly rich in future application scenarios for soft, intelligent and biodegradable robots. Figure 5 and Supplementary Video 10 demonstrate the potential for active interaction with a plant model by a 2-finger soft robotic gripper, which monitors the plant response to water stress and provides maintenance. The gripper could lift objects of various shapes weighing up to 100 g with sufficient mechanical force (Supplementary Fig. 31 and Supplementary Video 11). Figure 5a shows the operation of the biodegradable gripper incorporating Mg needles interconnected to the Mg electrodes using conductive wax (C-wax), composed of biodegradable tungsten particles and candelilla wax[37] (see Supplementary Fig. 32). The electrical impedance in the internal electrolyte was measured by the needles penetrating the centre of the *Monstera* plant stem while maintaining a consistent gripping force through a closed-loop control system with tactile feedback (Fig. 5b). Details of this closed-loop control system are provided in Supplementary Methods, Supplementary Notes and Supplementary Figs. 33 and 34. The impedance substantially dropped within 6 h after the plant was watered due to enhanced ion mobility, reduced intracellular resistance and increased cell tissue capacitance[38,39] (Fig. 5c). Figure 5d shows the gripper measuring both the leaf temperature and the surrounding air temperature, with a fingertip equipped with a temperature sensor repeatedly attaching and detaching from the plant leaf every 3 s. After watering, a decrease in leaf temperature compared to the surrounding air temperature was observed due to transpiration (Fig. 5e).

Figure 5f–h illustrates pruning using a Joule heater and wound protection using a drug-releasing device. The thin stem bent within 10 min after being heated (Fig. 5f). After 5 min of heating, the impedance rose dramatically, indicating complete combustion and stem mortality (Fig. 5g). On the other hand, an incision treated with a drug composed of cellulose mixed with antimicrobial silver microparticles (~10 µm) and gelatin hydrogel[40] remained more closed after 3 days compared with an untreated part (Fig. 5h). Additional information regarding the interaction demonstration between the robot and plants can be found in Supplementary Notes. The demonstrated configuration employed a few representative sensors from those presented earlier that clearly indicate specific parameters, while for other applications requiring more complex tasks, other combinations of sensors could be selectively employed. These preliminary studies suggest that our soft robotic gripper, capable of monitoring water stress, pruning and drug treatment, could be useful for enhancing agricultural and ornamental plant yields or managing forest environments.

Biodegradation of robotic finger

While biodegradable robots can, depending on their intended purpose, gradually decompose in vivo or in natural environments such as soil[1,5,8,12,13] and the ocean[4], we hypothesize that most discarded robots are likely to decompose rapidly into agricultural feedstock through industrial composting due to economic considerations. In principle, all inorganic components of our robotic system undergo hydrolysis to yield water-soluble hydroxide or oxide products, such as $Si(OH)_4$, $HMoO_4^-$ and $Mg(OH)_2$, whereas the organic components degrade via cleavage of ester bonds into shorter polymer chain segments (Supplementary Fig. 35). Moreover, the esterase produced by diverse microorganisms and the various chemicals in composting environments can accelerate polymer degradation and exert complex influences on the overall degradation behaviour of the constituent materials (Supplementary Notes). In particular, the biodegradable behaviour of inorganic materials comprising biodegradable electronics in composting environments has not been reported.

Consequently, we examined the changes in surface morphology (Fig. 6a) and thickness (Fig. 6b and Supplementary Fig. 36) of Mg, Mo and Si NM samples patterned by photolithography (Supplementary Fig. 37) when submerged in industrial compost conditions (pH 7–8, 58 °C and 100% humidity) as specified by international standards (ISO 14855-1) (Supplementary Fig. 38). Mg forms a white surface oxide layer of MgO and $Mg(OH)_2$ within 5 min of composting, which quickly dissolves, resulting in a dark grey appearance[41,42] (Fig. 6a). For Mo, surface oxide layers of yellow, light green and light blue (MoO_3) are observed after 5 h, 10 h and 20 h of composting, respectively[41–43]. Throughout the entire degradation process, Mg exhibits a highly non-uniform surface morphology, whereas Mo shows a relatively uniform morphology. Si also uniformly degrades across the entire surface, turning transparent and eventually disappearing. The degradation rates of Mg, Mo and Si were ~530 nm h^{-1}, 1.5 nm h^{-1} and 66 nm day^{-1}, respectively (Fig. 6b). In a composting environment, Mg, Mo and Si degrade ~7.6, ~5 and ~33 times faster, respectively, compared with their degradation rates in deionized water at room temperature environments[44–46]. The elevated temperatures in industrial composting conditions, along with enzymes and metabolites released by microorganisms present in the compost, are presumed to accelerate the degradation of inorganic materials[44–46].

Figure 6c and Supplementary Fig. 39 show the disintegration behaviour and morphological changes under industrial composting conditions. PGS, PBAT and PLA achieved ~100% disintegration in 19 days, 90 days and 80 days, respectively. PBTPA disintegrated by ~73.2% over 120 days. PGS achieved 100% ultimate aerobic biodegradation in 77 days, while PBAT, PLA and PBTPA underwent ~72.7%, ~73.2% and ~56.8% biodegradation after 120 days (Fig. 6d). The calculation method for the biodegradation percentage, based on CO_2 emissions, is described in Methods, Supplementary Table 3 and Supplementary Fig. 40. The biodegradation data for all polymers were fitted to the kinetic model[47] discussed in Supplementary Methods, Supplementary Notes and Supplementary Table 4. Accordingly, PBAT, PLA and PBTPA are expected to achieve ~90% biodegradation in 180 days, 220 days and 390 days, respectively (Supplementary Fig. 41).

The weight of the entire robotic finger decreased to ~13% of its initial weight after 90 days (Fig. 6e). The measured weights of the entire robotic finger during biodegradation closely matched the predicted weight, which was calculated on the basis of the weight percent (Supplementary Table 5) and degradation profiles of each individual constituent material. The robot almost completely disintegrated in the compost 100 days after the start of composting (Fig. 6f and Supplementary Fig. 42), and the resulting compost was then used immediately for a plant growth test according to the international standard (ISO 11269-2) (Fig. 6f and Supplementary Fig. 43). Similar levels of germination rate, survival rate, height and weight in the test compost compared to the control indicate that the by-products of the robot did not adversely affect plant growth, demonstrating carbon and nutrient cycling (see Supplementary Notes for details).

Discussion

Our compostable soft robot platform demonstrates that sustainability and performance in intelligent devices do not have to be mutually exclusive. Despite critical perceptions regarding the durability of biodegradable polymers, the 1,000,000-cycle actuation performance of the PGS actuator demonstrated the strong practical potential of biodegradable polymers as actuator materials. As demonstrated in this work, establishing a balanced design space that considers material properties, design optimization, operating environment and actuation range can accelerate the realization of highly durable biodegradable robots. Highly durable biodegradable robots not only reduce environmental impact at the end of their life cycle, but also minimize material and energy consumption during use by lowering replacement frequency. In this sense, they represent a direction that sustainable robotics should continue to pursue.

The high-performance inorganic transient electronics consisting of Mg, Mo and Si allowed active interaction based on real-time feedback control and treatment. The introduction of photolithography and transfer printing processes enabled the integration of electronic arrays with extremely small feature sizes and the incorporation of semiconductor materials (Si), which can be extended to more advanced electronics such as logic circuits. This suggests a strong potential for biodegradable electronics to replace the non-biodegradable inorganic electronics traditionally used in intelligent robots with minimal performance loss, while also mitigating issues of hazardous substance leakage at the end of life. Indeed, the plant growth tests showed that the composted by-products of robot devices containing biodegradable electronics can be integrated into the ecological environment without toxicity. Building on these characteristics, our platform can be extended to sustainable applications such as soil monitoring, crop

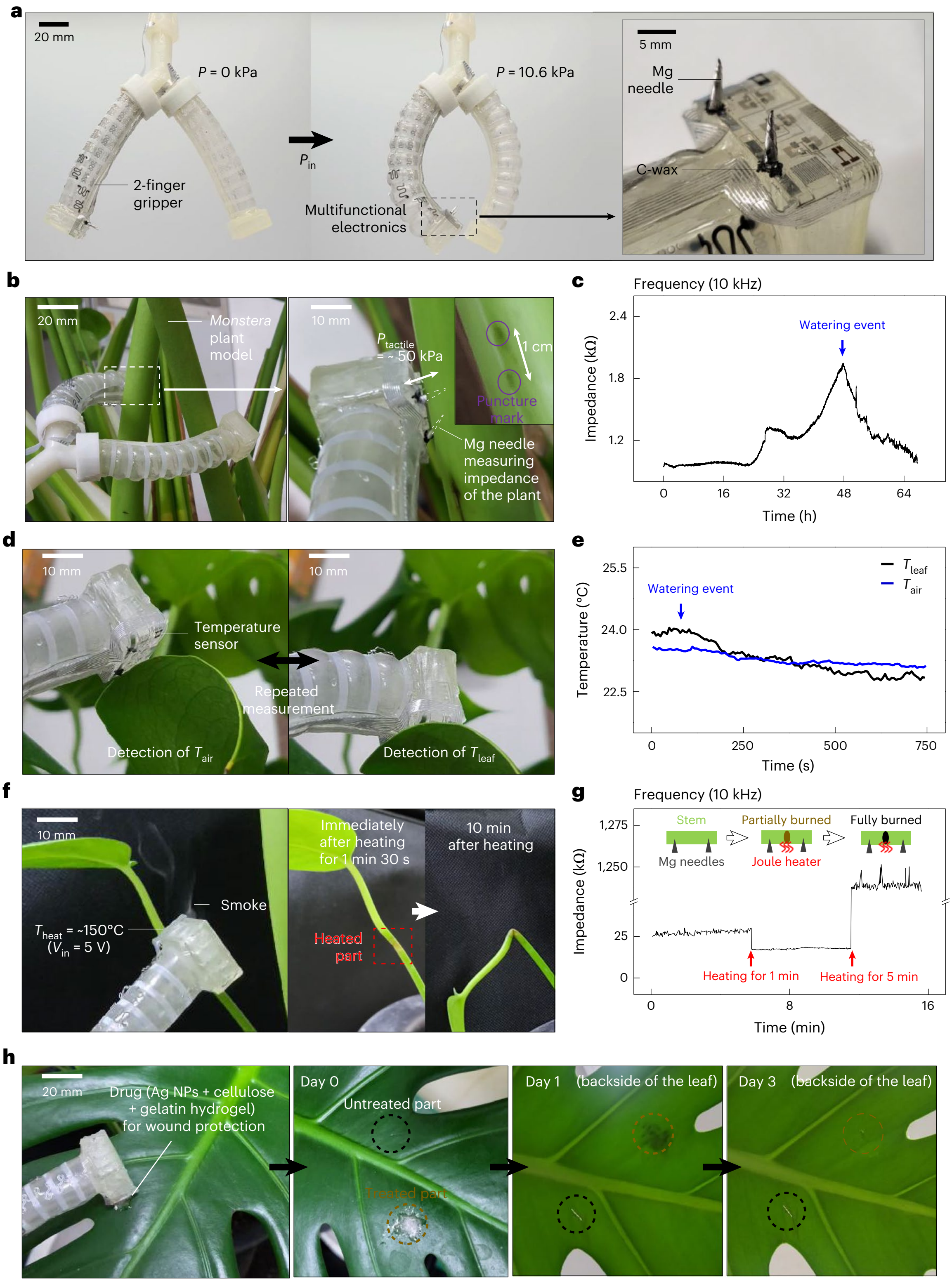

Fig. 5 | Biodegradable 2-finger soft gripper monitoring the condition of plants and providing plant care. a, Actuation of the biodegradable 2-finger soft gripper (left) integrated with Mg needles (right) functioning as probes for measuring the impedance of plants. **b**, Overall (left) and magnified (right) images of the soft gripper measuring the impedance of a plant model (*Monstera*) with controlled tactile pressure of ~50 kPa. The inset shows a puncture mark on the plant stem after the Mg needle was removed. **c**, Variation in the impedance of the plant model measured over 67 h before and after watering. **d**, Images of the soft gripper measuring temperature of the air (left) and a plant leaf (right), while repeatedly attaching to and detaching from the plant leaf. **e**, Variation in the temperature difference between the air and the plant leaf before and after watering. **f**, Images of the soft gripper pruning a plant stem using Joule heating (left) and the plant stem after being burnt and broken (right). **g**, Impedance changes measured by inserting two Mg needles into the stem, with the burning section in between. **h**, Soft gripper applying a drug to the damaged part of a plant leaf (far left) and the appearance of the plant leaf after 0 (middle left), 1 (middle right) and 3 (far right) days.

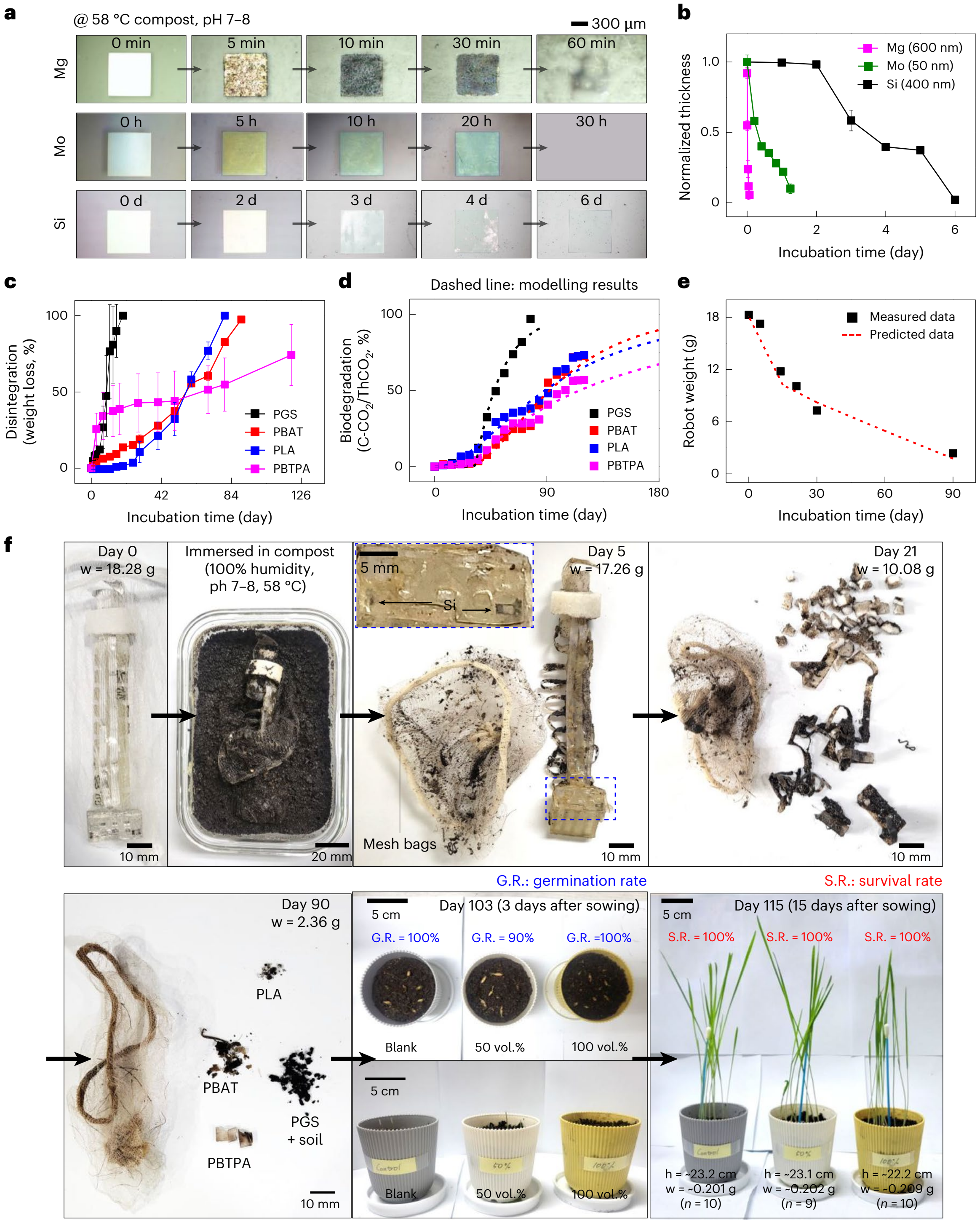

Fig. 6 | Biodegradation and eco-toxicity test of the soft robotic finger. **a**,**b**, Morphological change (**a**) and thickness change (**b**) of Mg (magenta), Mo (green) and Si (black) under industrial composting condition (100% humidity, 58 °C, pH 7–8) until complete dissolution. d, day. **c**,**d**, Weight loss (**c**) and ultimate biodegradation percentage (**d**) of PGS (black), PBAT (red), PLA (blue) and PBTPA (magenta) under industrial composting condition. **e**, Weight changes of the entire soft robotic finger over 90 days under industrial composting condition (measured data, black square; predicted data, red dotted line). **f**, Serial images of biodegradation and eco-toxicity test for the entire soft robotic finger. The robot degraded almost completely within 90 days under industrial composting condition (from top left to bottom left). The mesh bag was used to collect the disintegrated fragments for the disintegration assessment. When 10 oat seeds were planted in each of three pots for a comparative experiment (grey pot, control compost; white pot, control mixed with 50 vol.% of the sample-decomposed compost; yellow pot, only the sample-decomposed compost) (bottom middle), the plants showed no major differences in size or weight (bottom right). **b**,**c**, Data are presented as mean ± s.d. of *n* = 3 independent measurements. **f**, Out of 10 plants at 50 vol.%, one did not germinate, so the average height and weight data are presented for the remaining 9 plants.

management or exploration of remote forest areas where device retrieval is challenging.

Further work on functional materials such as photo-curable and biodegradable PGS could facilitate the production of more uniform and versatile elastomer films, overcoming current challenges such as the excessively sticky nature and inconsistent curing of PGS (Supplementary Fig. 44). These improvements would enable the use of sustainable fabrication methods, such as moulding and 3D printing, that minimize raw material loss during robot manufacture. Our soft robotic gripper exhibited a weight-lifting ratio of ~6.29 and a maximum blocking force of 1 N, but there remains room to enhance energy efficiency through higher force output. Further research is required to enhance their force output through various strategies, including increasing the toughness of the elastic material via optimization of crosslinkers, chain extenders, lubricants and particle fillers, reinforcing the structure using fibres or fabrics, and filling the chambers with liquids such as water or oil instead of air. Moreover, the implementation of untethered actuation through additional components would substantially enhance mobility, expanding the scope of applications beyond the limitations of tethered systems. Beyond simple pneumatic actuation, achieving complete biodegradability in conventional robotic components such as motors, batteries and microprocessors is necessary, and with further technological advancements in this area, it would be possible to develop fully sustainable soft robotic platforms. Such systems, capable of actuation, sensing, power generation and control, could revolutionize fields such as healthcare and exploration by enabling highly adaptive, perceptive soft robots equipped with advanced electronic components.

Methods

Preparation of PGS and PBTPA

The PGS pre-polymer was synthesized by microwaving a mixture of 4.605 g of glycerol (Sigma-Aldrich) and 10.113 g of sebacic acid (SAMCHUN) in a 1:1 molar ratio for 4 min in a 30 ml vial[48,49]. The pre-polymer was poured into a self-assembled monolayer (SAM) surface-treated dish, which had been treated with an octadecyltrimethoxysilane solution (100 µl, Sigma-Aldrich) in hexane (60 ml, DAEJUNG) for 1.5 h. The polymer was subsequently cured at 120 °C under 0.1 torr for 14 h. Only the 14-h-cured PGS polymer was used for the soft actuators due to its high elongation properties. For comparison of mechanical properties, PGS samples were also prepared by curing for 19 and 24 h (Supplementary Fig. 1).

The liquid-state PBTPA adhesive was prepared by mixing 4-pentenoic anhydride (4PA) (Sigma-Aldrich), 1,3,5-triallyl-1,3,5-triazine-2,4,6(1H,3H,5H)-trione (TTT) (Sigma-Aldrich) and 1,4-butanedithiol (BDT) (Sigma-Aldrich) in a molar ratio of 1:4:7, along with 0.4 wt% of 2,2-dimethoxy-2-phenylacetophenone (Sigma-Aldrich) as a photoinitiator. To obtain the rigid-state PBTPA polymer, the adhesive was cured under UV light (364 nm).

Fabrication of the PGS-framed bending actuator

The cured PGS sheet was cut to dimensions of 44 mm × 68 mm to form the robot body for bending (Supplementary Figs. 6 and 7). A PBAT film (~100 µm thick) was formed by evaporating a solution of PBAT (1 g, SEnPol) and chloroform (10 ml, DAEJUNG) on the SAM surface-treated slide glass. The film was then patterned into the shape of a strain limiter using laser cutting and rolled into a cylindrical shape along with the PGS sheet. A viscous PBTPA pre-polymer was applied to the joint of the cylindrical body and cured under UV light (364 nm) for firm fixation. The cylindrical body, PBTPA block and 3D-printed PLA (Woomin 3D Printing) connector were assembled using PBTPA adhesive.

Fabrication of the robotic finger with electronics

Supplementary Figs. 15–21 show the detailed fabrication process and component specifications of the proprioceptive bendable actuator and multifunctional electronic fingertip. A 30-µm-thick Mg foil was attached to the PGS sheet and PBAT film, then patterned into the shape of the serpentine strain sensors and interconnecting lines using laser cutting (3 W, 50 kHz, 50 mm s^{-1}) (MD-U1000C, Keyence) (step 1 of Supplementary Fig. 15). Local strain sensors, made from 80-µm-thick Mo/PBAT, were attached to the PGS sheet and interconnected with the Mg interconnecting lines by a heating process (step 2 of Supplementary Figs. 15 and 16a–c). The Mo/PBAT film (~80 µm thick) was prepared by casting a Mo/PBAT (Mo 35 vol.%) paste solution onto a glass substrate. This paste was formed by mixing Mo particles (5–100 µm, Aladdin) with a 20% w/v PBAT/chloroform solution using a centrifugal mixer (ARE-310, Thinky). The Mo/PBAT sheet was patterned into the shape of the serpentine local strain sensors using laser cutting (3 W, 50 kHz, 50 mm s^{-1}). A PBAT film (~100 µm thick) was patterned into the shape of a strain limiter by laser cutting and rolled into a cylindrical structure along with the PGS sheet, Mg foil and Mo/PBAT sensors (step 3, Supplementary Figs. 15 and 16d). A PBTPA pre-polymer was applied to the joint of the cylindrical body and cured under UV light (364 nm) for firm fixation (step 4 of Supplementary Fig. 15).

A PLA (Woomin 3D Printing) mould was printed via fused deposition modelling using a 3D printer (DP200, Sindoh). The mould was immersed in a PDMS pre-polymer, and after curing at 60 °C, the PLA structure was removed. The PBTPA pre-polymer was then poured into the PDMS mould and cured to fabricate the PBTPA block and PBTPA trench (step 5, Supplementary Fig. 15). The PBTPA block was used to seal the cylindrical body, with additional PBTPA adhesive cured under UV light (step 6, Supplementary Fig. 15). The PBTPA trench, which enhances the sensitivity of tactile sensors (Supplementary Fig. 17a,b), was attached to the PBTPA block using PBTPA adhesive (step 6, Supplementary Fig. 15).

A 30-µm-thick Mg foil was placed on a 100-µm-thick PBAT substrate, patterned through laser cutting (3 W, 50 kHz, 50 mm s^{-1}) and adhered by heating at 200 °C. The Mg foil was patterned into the shapes of an electrical stimulator, humidity sensor, Joule heater and interconnecting wires by laser cutting. Unpatterned regions of the Mg foil were removed (step 7, Supplementary Fig. 15).

A 12.5-µm-thick polyimide film was patterned as a shadow mask for Mo crack-based tactile sensors and attached to the PBAT film. A 15 nm layer of MoO_3 was deposited on the PBAT film as an adhesion layer, and 50 nm of Mo was deposited with a shadow mask via sputtering (J Vacuum Technology) (step 8, Supplementary Fig. 15). After removing the polyimide film, tactile sensing element arrays were fabricated through crack formation induced by repetitive stretching (step 9, Supplementary Fig. 15). All tactile sensing elements were interconnected using Mg wires on the PBAT substrate via conductive wax (C-wax)[37], composed of biodegradable tungsten particles (5 µm, US Research Nanomaterials) at a ratio of 40 vol.% in candelilla wax (Koreasimilac) (Supplementary Fig. 17c).

To fabricate the pH sensor, a piece of SOI wafer (top silicon ~400 nm, SOITEC) was spin coated (3,000 r.p.m., 30 s) with a boron dopant (B153, Filmtronics) and doped at 1,050 °C for 20 min using a furnace (LF-GT630, LK LAB) (Supplementary Fig. 18). The wafer was functionalized by immersion in a 1% ethanol solution of APTES (Sigma-Aldrich) for 20 min, rinsed with ethanol three times and heated at 80 °C for 10 min[26]. The p-doped pH sensors were patterned using photoresist (MicroChemicals) and isolated using a reactive ion etcher (J Vacuum Technology) with SF_6 gas. The SOI wafer was immersed in hydrofluoric acid to remove the buried oxide layer, and the separated silicon patterns were transferred to a predetermined location on the PBAT substrate using a PDMS stamp (SYLGARD 184, Dow Chemical) and ethyl acetate (Sigma-Aldrich) (step 10, Supplementary Fig. 15).

A temperature-sensing diode was fabricated by depositing an SiO_2 layer (~600 nm thick) via PECVD (Oxford PECVD, PlasmaPro 100) on a piece of SOI wafer (Supplementary Fig. 19). The p-doped region was patterned using an aligner (MDA-400S, MIDAS), and the patterned oxide was etched using buried oxide etchant (BOE, SAMCHUN). Boron doping was performed at 1,050 °C for 20 min, followed by thermal oxide removal using hydrofluoric acid (SAMCHUN) and nano-strip (CMC Materials). The n-doping of the diode was carried out with a phosphorus dopant (P509, Filmtronics) at 1,050 °C for 5 min after patterning. The diode components were transferred to the PBAT substrate in the same manner as the pH sensors (step 10, Supplementary Fig. 15). Mo pads (~300 nm thick) for interconnecting the diodes were deposited onto the PBAT film using a polyimide film shadow mask via sputtering (step 11, Supplementary Fig. 15).

Gelatin hydrogels for the drug reservoir were prepared by mixing blue dye, gelatin powder (Sigma-Aldrich) and deionized water. For the wound-healing demonstration in Fig. 4h, cellulose microparticles (Sigma-Aldrich) and silver flakes (Sigma-Aldrich) were added to the hydrogel. The hydrogel, cast to a thickness of 1 mm, was cut into 3 mm × 5 mm pieces and thermally bonded onto the Joule heater as a drug reservoir (step 12, Supplementary Fig. 15). Images of all electronics integrated on the PBAT substrate are provided in Supplementary Fig. 20.

Finally, the fingertip with multiple sensors was fabricated by covering the top PBTPA encapsulation layer and PBTPA bumps, and fixing them with PBTPA adhesive (step 12, Supplementary Fig. 15). This step allowed the fingertip to contain a micro electro mechanical system (MEMS)-structured tactile sensor using PBTPA trenches and PBTPA bumps (Supplementary Fig. 17). The interconnecting wire parts were laminated onto the strain-limiting region using PBTPA adhesive (step 13, Supplementary Fig. 15). The PLA connector (consisting of a PLA cover and PBTPA-coated PLA pipe) was laminated onto the top part of the cylindrical body using PBTPA adhesive (step 14, Supplementary Fig. 15). Detailed dimensions of all parts are described in Supplementary Fig. 21.

Measurement of mechanical properties of the polymers

The mechanical properties of the PGS, PBAT and PBTPA specimens, prepared according to the sample specifications presented in ISO 527-2:2012, were measured using a tensile testing machine (68TM-5, Instron 3343) with Instron Bluehill2 software. The tests were conducted with a 50 N load cell at a strain rate of 50% min^{-1}. To evaluate storage stability, samples were stored under laboratory conditions (room temperature, ambient environment) for periods of 30, 90 and 180 days.

Characterization of the biodegradable soft actuator

The inflation trajectory (that is, bending angle) of the PGS-framed bending actuator was measured using video analysis software (Tracker) (Supplementary Fig. 45). Displacement data along the X and Y axes, obtained from a trackable point at the centre of the actuator tip, were converted into bending angles using the arctangent function. The blocking force, the maximum force produced when the displacement of the actuator is fully restricted, was measured using a force gauge attached to a tensile testing machine (ElectroPuls E10000, Instron). During force measurement, the deformation of the PGS-framed bending actuator was constrained by an external rigid pipe, following previously reported methods for measuring the force of soft actuators[5]. The actuators were inflated and deflated using a syringe pump (TYD01-01, Leadfluid) at a rate of ~0.93 ml s^{-1} during the measurement of bending angles and blocking forces. For each cycle, a bending angle of 0° to ~50° was achieved by varying the internal air pressure from 0 to 10.6 kPa. In the durability test involving 1,000,000 actuation cycles within a bending angle range of 0°–50°, the speed of the cycles was accelerated except during the 1st, 10th, 100th, 1,000th, 10,000th, 100,000th and 1,000,000th cycles, during which performance was measured. The syringe pump speed was set to ~4.67 ml s^{-1}, ensuring that each cycle was completed within ~3 s, with the total test duration kept within 35 days. To evaluate storage stability, the PGS-bending actuators were stored under laboratory conditions (room temperature, ambient environment) for periods of 180 days.

Evaluation of the various electronics

The Mg capacitive strain sensor, used to measure curvature, was evaluated while integrated into a soft actuator that was inflated and deflated by a syringe pump at a rate of ~0.93 ml s^{-1}. To calibrate the capacitance values on the basis of the bending angle, an onboard circuit was prepared (Supplementary Fig. 33b). Since directly tracking the bending angle involves complex data processing, air pressure, which can be easily measured using a pressure sensor, was used to infer bending angle values through a fitting equation (Supplementary Fig. 46). By utilizing the ~25 pF stray capacitance inherent in the Arduino Uno microcontroller board, the capacitance values of the sensors connected to pins A0 and A2 were measured. PLX-DAQ software was used for real-time data readout.

Direct observation of the strain distribution in the PGS-framed bending actuator is challenging, making it difficult to accurately calibrate electrical resistance in response to strain when the Mo/PBAT local strain sensor is integrated into the soft actuator. To obtain a calibration curve for the Mo/PBAT sensor, a specimen was prepared by attaching the sensor to a piece of PGS measuring 10 mm × 50 mm and connecting it with a Mg foil-based wire. The specimen was uniaxially stretched at a rate of 50% s^{-1} using a tensile machine (ElectroPuls E10000, Instron) and returned to its original state, while resistance changes were recorded with a digital multimeter (USB-4065, National Instruments) and LabVIEW SignalExpress software.

The tactile sensors were evaluated while integrated into a soft robotic finger. To calibrate the tactile sensors, a maximum external force of 1.2 N was applied to the PBTPA bump using the compression mode of a tensile machine (ElectroPuls E10000, Instron) at a rate of 0.4 N s^{-1}. During this process, changes in resistance were recorded with a digital multimeter.

The pH sensor was evaluated by measuring its conductance with a digital multimeter (USB-4065, National Instruments) after adding a drop of buffer solution with pH levels ranging from 4 to 9 onto the pH sensor. The sensing ability of the pH sensor was confirmed by variations in conductance corresponding to changes in pH.

The temperature sensor was evaluated by obtaining the I–V curve of the diode using a probe station (customized, MS Tech) with 4200A-SCS Clarius+ software while varying the temperature from 35 to 65 °C in 5 °C increments. The sensing ability was verified by observing changes in diode current at a fixed voltage (1 V).

The humidity sensor was calibrated by measuring the change in capacitance in response to varying internal moisture levels of a gelatin hydrogel in contact with the sensor, using a custom-made onboard circuit.

Thermal distribution images during the operation of the Joule heater and the drug release device were captured using a thermal camera (FLIR A6700 MWIR, Teledyne FLIR) and FLIR ResearchIR Max software.

Impedance measurements of Mg needles were performed using an impedance analyser (Zive MP2A, WonaTech) at a fixed frequency of 10,000 Hz. Before measurement, the plant was not watered to ensure maximum water stress conditions.

Evaluation of the ultimate aerobic biodegradation

Details about the evaluation process for the disintegration of biodegradable polymers can be found in Supplementary Methods. The biodegradation tests for polymers under aerobic composting conditions were conducted in accordance with the ISO standard (ISO 14855-1:2012). An overview of the biodegradation test setup is shown in Supplementary Fig. 38a,b. Compost was collected from a farm facility (Tae Min Nongjajae). The activity of the compost was confirmed as the reference material (cellulose) exhibited 70% biodegradation within 45 days (Supplementary Fig. 38c). The cellulose sample was prepared in powder form (Sigma-Aldrich). PGS and PBTPA samples were prepared by cutting polymer sheets, while PLA and PBAT samples were formed into pellets. Test materials of 10 g were mixed with 60 g of compost and placed into a bioreactor maintained at a temperature of 58 ± 2 °C. The moisture content of the compost was adjusted to 50% by adding deionized water. Carbon dioxide from the ambient air was removed by passing it through a sodium hydroxide solution (0.5 M), ensuring that only the carbon dioxide released from the decomposition of the samples was captured in the final sodium hydroxide solution, also at a concentration of 0.5 M.

Carbon dioxide generated from the biodegradation of the polymers in the bioreactor was captured in the final sodium hydroxide solution, and 10 ml samples were stored in 15 ml vials every 2 days. Cumulative carbon dioxide production was analysed weekly using a total organic carbon (TOC) analyser (TOC-VCPH, Shimadzu). For analysis, samples were diluted by mixing 1 ml with 19 ml of deionized water in a 20 ml vial, resulting in a 20-fold dilution. TOC calibration samples for total carbon were prepared by dissolving 0.2125 g of potassium hydrogen phthalate ($C_8H_5KO_4$) in 100 ml of deionized water to make a 100 ppm solution, which was then diluted to 1, 5, 10, 25 and 50 ppm. For inorganic carbon, a 100 ppm solution was prepared by dissolving 0.4415 g of sodium carbonate (Na_2CO_3) and 0.35 g of sodium bicarbonate ($NaHCO_3$) in 100 ml of deionized water, which was then diluted to 1, 5, 10, 25 and 50 ppm.

The biodegradation rate of the test polymers was calculated by comparing the amount of carbon dioxide detected from the decomposition of the materials to the theoretical amount of carbon dioxide that could be released from complete decomposition. The theoretical amount of carbon dioxide ($ThCO_2$) produced by the test materials was calculated (Supplementary Fig. 40) using the following formula:

$$\mathrm{ThCO_2} = M_{\mathrm{tot}} \times C_{\mathrm{tot}} \times \frac{44}{12} \quad (1)$$

where, M_{tot} is the initial weight of the test polymer (g). C_{tot} is the total carbon content of the test polymer ($\mathrm{g\,g^{-1}}$). The values 44 and 12 represent the molecular weights of carbon dioxide and carbon, respectively. The theoretical amount of carbon dioxide was verified using an elemental analyser (FLASH 2000 CHNS/O Analyzer, Thermo Fisher) (Supplementary Table 3). The amount of carbon dioxide generated from sample biodegradation was measured using a total organic carbon analyser.

The biodegradation rate of the test polymers at each interval was calculated using the following formula:

$$\mathrm{Biodegradation\,(\%)} = \frac{\mathrm{CO_2total} - \mathrm{CO_2blank}}{\mathrm{ThCO_2}} \quad (2)$$

where, CO_2total is the cumulative amount of carbon dioxide produced by each bioreactor, CO_2blank is the cumulative amount of carbon dioxide produced by the blank bioreactor.

Evaluation of biodegradation of transient inorganics

For the preparation of inorganic samples for biodegradation tests, Mg (~600 nm thick) and Mo (~50 nm thick) were sputtered and patterned into square shapes (700 × 700 μm) onto glass slides using photolithography and lift-off techniques. Si NMs (~400 nm thick) were patterned onto the buried oxide (BOX) layer of a SOI wafer (Supplementary Fig. 37). The glass substrate and BOX layer served as baselines for thickness measurement due to their negligible degradation under composting conditions of pH 7–8 (ref. 47). To prevent peeling during the biodegradation test, a Cr layer (~10 nm thick), deposited by sputtering, was used as an adhesion promoter. The inorganic samples were mixed with compost and placed in a bioreactor maintained at 58 ± 2 °C. The thin metal films and Si NMs were immersed in the composting environment, and the changes in thickness over time were measured using profilometry (DektakXT, Bruker). The degradation rates were defined as the value obtained by dividing the initial thickness by the time required for complete dissolution[25,42,50].

Reporting summary

Further information on research design is available in the Nature Portfolio Reporting Summary linked to this article.

Data availability

Source data are provided with this paper. All data generated or analysed during this study are included in the paper. Source data are provided with this paper.

References

1. Rumley, E. H. et al. Biodegradable electrohydraulic actuators for sustainable soft robots. *Sci. Adv.* **9**, adf5551 (2023).
2. Mazzolai, B. et al. A vision for future bioinspired and biohybrid robots. *Sci. Robot.* **5**, aba6893 (2020).
3. Laschi, C. et al. Soft robotics: technologies and systems pushing the boundaries of robot abilities. *Sci. Robot.* **1**, aah3690 (2016).
4. Mazzolai, B. et al. Roadmap on soft robotics: multifunctionality, adaptability and growth without borders. *Multifunct. Mater.* **5**, 032001 (2022).
5. Hartmann, F. et al. Becoming sustainable, the new frontier in soft robotics. *Adv. Mater.* **33**, 2004413 (2020).
6. Baumgartner, M. et al. Resilient yet entirely degradable gelatin-based biogels for soft robots and electronics. *Nat. Mater.* **19**, 1102–1109 (2020).
7. Heiden, A. et al. 3D printing of resilient biogels for omnidirectional and exteroceptive soft actuators. *Sci. Robot.* **7**, eabk2119 (2022).
8. Kanno, R. et al. Biodegradable electrohydraulic soft actuators. *Adv. Intell. Syst.* **5**, 2200239 (2023).
9. Xu, C. et al. Novel dielectric elastomer actuator based on compliant polyvinyl alcohol hydrogel electrodes. *J. Mater. Sci. Mater. Electron.* **26**, 9213–9218 (2015).
10. Duan, J. et al. Bilayer hydrogel actuators with tight interfacial adhesion fully constructed from natural polysaccharides. *Soft Matter* **13**, 345–354 (2017).
11. Han, W. B. et al. Ultra-stretchable and biodegradable elastomers for soft, transient electronics. *Nat. Commun.* **14**, 2263 (2023).
12. Wiesemüller, F. et al. Biopolymer cryogels for transient ecology-drones. *Adv. Intell. Syst.* **5**, 2300037 (2023).
13. Cikalleshi, K. et al. A printed luminescent flier inspired by plant seeds for eco-friendly physical sensing. *Sci. Adv.* **9**, adi8492 (2023).
14. Cianchetti, M. et al. Biomedical applications of soft robotics. *Nat. Rev. Mater.* **3**, 143–153 (2018).
15. Aracri, S. et al. Soft robots for ocean exploration and offshore operations: a perspective. *Soft Robot.* **8**, 625–639 (2021).
16. Armanini, C. et al. Soft robotics for farm to fork: applications in agriculture and farming. *Bioinspir. Biomim.* **19**, 021002 (2024).
17. Zhang, M. et al. Synthesis of poly(l-lactide-co-ε-caprolactone) copolymer: structure, toughness, and elasticity. *Polymers* **13**, 1270 (2021).
18. Yu, L. et al. Development of poly(1,8-octane diol-co-citrate-co-ascorbate) elastomers with enhanced ascorbate performance for use as a graft coating to prevent neointimal hyperplasia. *ACS Appl. Bio Mater.* **3**, 2150–2159 (2020).
19. Webb, A. R. et al. Biodegradable poly(diol citrate) nanocomposite elastomers for soft tissue engineering. *J. Mater. Chem.* **17**, 900–906 (2007).
20. Barrioni, B. R. et al. Synthesis and characterization of biodegradable polyurethane films based on HDI with hydrolyzable crosslinked bonds and a homogeneous structure for biomedical applications. *Mater. Sci. Eng. C Mater. Biol. Appl.* **52**, 22–30 (2015).

21. Hsu, S. H. et al. Novel flexible nerve conduits made of water-based biodegradable polyurethane for peripheral nerve regeneration. *J. Biomed. Mater. Res. A* **105**, 1383–1392 (2017).
22. Wang, C. et al. A novel biodegradable polyurethane based on poly(3-hydroxybutyrate-co-3-hydroxyvalerate) and poly(ethylene glycol) as promising biomaterials with the improvement of mechanical properties and hemocompatibility. *Polym. Chem.* **7**, 6120–6132 (2016).
23. Aydin, H. M. et al. Microwave-assisted rapid synthesis of poly(glycerol-sebacate) elastomers. *Biomater. Sci.* **1**, 503–509 (2013).
24. Chen, C. et al. A foil-based additive manufacturing technology for metal parts. *J. Manuf. Sci. Eng.* **139**, 024501 (2016).
25. Hwang, S. W. et al. A physically transient form of silicon electronics. *Science* **337**, 1640–1644 (2012).
26. Hwang, S. W. et al. Biodegradable elastomers and silicon nanomembranes/nanoribbons for stretchable, transient electronics, and biosensors. *Nano Lett.* **15**, 2801–2808 (2015).
27. Hwang, S. W. et al. Materials and fabrication processes for transient and bioresorbable high-performance electronics. *Adv. Funct. Mater.* **23**, 4087–4093 (2013).
28. Hwang, S. W. et al. High-performance biodegradable/transient electronics on biodegradable polymers. *Adv. Mater.* **26**, 3905–3911 (2014).
29. Kang, D. et al. Ultrasensitive mechanical crack-based sensor inspired by the spider sensory system. *Nature* **516**, 222–226 (2014).
30. Kim, Y. et al. Capacitive humidity sensor design based on anodic aluminum oxide. *Sens. Actuators B Chem.* **141**, 441–446 (2009).
31. Tabrizian, S. K. et al. A healable resistive heater as a stimuli-providing system in self-healing soft robots. *IEEE Robot. Autom. Lett.* **7**, 4574–4581 (2022).
32. Tang, S. et al. Enzyme-powered Janus platelet cell robots for active and targeted drug delivery. *Sci. Robot.* **5**, eaba6137 (2020).
33. Hwang, G. et al. Catalytic antimicrobial robots for biofilm eradication. *Sci. Robot.* **4**, eaaw2388 (2019).
34. Urso, M. et al. Smart micro- and nanorobots for water purification. *Nat. Rev. Bioeng.* **1**, 236–251 (2023).
35. Li, M. et al. Soft actuators for real-world applications. *Nat. Rev. Mater.* **7**, 235–249 (2022).
36. Kondoyanni, M. et al. Bio-inspired robots and structures toward fostering the modernization of agriculture. *Biomimetics* **7**, 69 (2022).
37. Won, S. M. et al. Natural wax for transient electronics. *Adv. Funct. Mater.* **28**, 1801819 (2018).
38. Garlando, U. et al. Ask the plants directly: understanding plant needs using electrical impedance measurements. *Comput. Electron. Agric.* **193**, 106707 (2022).
39. Jócsák, I. et al. Electrical impedance measurement on plants: a review with some insights to other fields. *Theor. Exp. Plant Physiol.* **31**, 359–375 (2019).
40. Alonso-Díaz, A. et al. Enhancing localized pesticide action through plant foliage by silver-cellulose hybrid patches. *ACS Biomater. Sci. Eng.* **5**, 413–419 (2019).
41. Shim, J. S. et al. Physically transient electronic materials and devices. *Mater. Sci. Eng. R Rep.* **145**, 100624 (2021).
42. Yin, L. et al. Dissolvable metals for transient electronics. *Adv. Funct. Mater.* **24**, 645–658 (2014).
43. Badawy, W. A. et al. Corrosion and passivation behaviors of molybdenum in aqueous solutions of different pH. *Electrochim. Acta* **44**, 693–702 (1998).
44. Liang, T. et al. Insight into microbiologically induced corrosion performance of magnesium in tryptic soy broth with *S. aureus* and *E. coli*. *J. Mater. Sci. Technol.* **115**, 221–231 (2022).
45. Guo, Z. et al. *Pseudomonas aeruginosa*-accelerated corrosion of Mo-bearing low-alloy steel through molybdenum-mediating chemotaxis and motility. *Bioelectrochemistry* **144**, 108047 (2022).
46. Dierksen, D. et al. Microbial corrosion of silicon nitride ceramics by sulphuric acid producing bacteria *Acidithiobacillus ferrooxidans*. *J. Eur. Ceram. Soc.* **31**, 1177–1185 (2011).
47. Leejarkpai, T. et al. Biodegradable kinetics of plastics under controlled composting conditions. *Waste Manage.* **31**, 1153–1161 (2011).
48. Wang, Y. et al. A tough biodegradable elastomer. *Nat. Biotechnol.* **20**, 602–606 (2002).
49. Wu, Z. et al. Effect of curing time on the mechanical properties of poly (glycerol sebacate). *J. Appl. Polym. Sci.* **140**, e53700 (2023).
50. Kang, S. K. et al. Dissolution behaviors and applications of silicon oxides and nitrides in transient electronics. *Adv. Funct. Mater.* **24**, 4427–4434 (2014).

Acknowledgements

This work was supported by National Research Foundation of Korea (NRF) grant RS-2025-02305569 (S.-K.K.) and 2022M3H4A1A04096393 (S.-K.K.) funded by the Ministry of Science and ICT.

Author contributions

K.-S.K., J.-S.S., J.-Y.B., M.-H.O., J.-Y.L., J.-H.L., S.-G.C., S.-M.L., S.-H.K., J.-H.P., R.K.-B., S.Y.K. and S.-K.K. conceptualized, designed and fabricated soft actuators, soft electronics and their interfaces. K.-S.K., S.-W.K., M.-S.C., S.-Y.C., J.-Y.S. and S.-K.K. conceptualized and conducted evaluations of the mechanical properties of polymers and the durability of actuators. G.-S.H., J.-h.K. and J.-Y.K. performed FEA simulation. K.-S.K. and J.B. developed software for robot control. K.-S.K., J.-S.S., S.-W.K., M.-S.C., J.J., J.J.K., J.K.H, K-S.L. and S.-K.K. specified and conducted applicable demonstrations of the biodegradable robots. K.-S.K., S.-W.K., Y-J.P., M.-J.C., Y.-S.K., Y.-W.K., W-J.L., I.-D.K., K.-H.K., M.-R.O., M.K. and S.-K.K. designed and conducted biodegradation and eco-toxicity evaluation experiments. K-S.K., J.-S.S., S.-W.K., G.-S.H., Y.-J.P., R.K.-B., S.-Y.K., M.K. and S.-K.K. wrote and revised manuscripts.

Competing interests

The authors declare no competing interests.

Additional information

Supplementary information The online version contains supplementary material available at https://doi.org/10.1038/s41893-026-01780-4.

Correspondence and requests for materials should be addressed to Sang Yup Kim, Martin Kaltenbrunner or Seung-Kyun Kang.

Peer review information *Nature Sustainability* thanks the anonymous reviewer(s) for their contribution to the peer review of this work.

[1]Department of Materials Science and Engineering, Seoul National University, Seoul, Republic of Korea. [2]Research Institute of Advanced Materials (RIAM), Seoul National University, Seoul, Republic of Korea. [3]Department of Materials Science and Engineering, UNIST (Ulsan National Institute of Science and Technology), Ulsan, Republic of Korea. [4]Department of Mechanical Engineering and Materials Science, Yale University, New Haven, CT, USA. [5]Department of Materials Science and Engineering, Pukyong National University, Busan, Republic of Korea. [6]Biomedical Engineering Research Center, Asan Medical Center, College of Medicine, University of Ulsan, Seoul, Republic of Korea. [7]Institute of Tissue Regeneration Engineering (ITREN), Dankook University, Cheonan, Republic of Korea. [8]Soft Foundry Institute, Seoul National University, Seoul, Republic of Korea. [9]Biomaterials Research Center, Biomedical Research Division, Korea Institute of Science and Technology (KIST), Seoul, Republic of Korea. [10]Division of Bio-Medical Science and Technology KIST School, Korea University of Science and Technology, Seoul, Republic of Korea. [11]Flexible Electronics Research Section, Reality Devices Research Division, Hyper-Reality Metaverse Research Laboratory, Electronics and Telecommunications Research Institute (ETRI), Daejeon, Republic of Korea. [12]Department of Physical Medicine and Rehabilitation, Ajou University School of Medicine, Suwon, Republic of Korea. [13]Department of Mechanical Engineering, Sogang University, Seoul, Republic of Korea. [14]Division of Soft Matter Physics, Institute for Experimental Physics, Johannes Kepler University, Linz, Austria. [15]Soft Materials Lab, Linz Institute of Technology, Johannes Kepler University, Linz, Austria. [16]Interdisciplinary Program of Bioengineering, Seoul National University, Seoul, Republic of Korea. [17]These authors contributed equally: Kyung-Sub Kim, Jun-Seok Shim, Sung-Woo Kim. ✉e-mail: sangyupkim@sogang.ac.kr; m.w.kaltenbrunner@jku.at; kskg7227@snu.ac.kr

nature portfolio

Corresponding author(s): Seung-Kyun Kang

Last updated by author(s): May 1, 2025

Reporting Summary

Nature Portfolio wishes to improve the reproducibility of the work that we publish. This form provides structure for consistency and transparency in reporting. For further information on Nature Portfolio policies, see our Editorial Policies and the Editorial Policy Checklist.

Statistics

For all statistical analyses, confirm that the following items are present in the figure legend, table legend, main text, or Methods section.

n/a	Confirmed	
☐	☒	The exact sample size (n) for each experimental group/condition, given as a discrete number and unit of measurement
☐	☒	A statement on whether measurements were taken from distinct samples or whether the same sample was measured repeatedly
☒	☐	The statistical test(s) used AND whether they are one- or two-sided *Only common tests should be described solely by name; describe more complex techniques in the Methods section.*
☒	☐	A description of all covariates tested
☒	☐	A description of any assumptions or corrections, such as tests of normality and adjustment for multiple comparisons
☐	☒	A full description of the statistical parameters including central tendency (e.g. means) or other basic estimates (e.g. regression coefficient) AND variation (e.g. standard deviation) or associated estimates of uncertainty (e.g. confidence intervals)
☒	☐	For null hypothesis testing, the test statistic (e.g. F, t, r) with confidence intervals, effect sizes, degrees of freedom and P value noted *Give P values as exact values whenever suitable.*
☒	☐	For Bayesian analysis, information on the choice of priors and Markov chain Monte Carlo settings
☒	☐	For hierarchical and complex designs, identification of the appropriate level for tests and full reporting of outcomes
☒	☐	Estimates of effect sizes (e.g. Cohen's d, Pearson's r), indicating how they were calculated

Our web collection on statistics for biologists contains articles on many of the points above.

Software and code

Policy information about availability of computer code

Data collection	Instron Bluehill2 - mechanical test, actuator force measurement; LabVIEW SignalExpress - strain, pH, tactile pressure measurement; PLX-DAQ (Arduino) - curvature, humidity measurement; 4200A-SCS Clarius+ Software - PIN diode characterization; FLIR ResearchIR Max - infrared images capture
Data analysis	ABAQUS - mechanical anaylsis ; Origin Pro 9.0, Excel - analyze and plot the data; Rhinoceros 5 and Keyshot 6 - illustrations

For manuscripts utilizing custom algorithms or software that are central to the research but not yet described in published literature, software must be made available to editors and reviewers. We strongly encourage code deposition in a community repository (e.g. GitHub). See the Nature Portfolio guidelines for submitting code & software for further information.

Data

Policy information about availability of data

All manuscripts must include a data availability statement. This statement should provide the following information, where applicable:

- Accession codes, unique identifiers, or web links for publicly available datasets
- A description of any restrictions on data availability
- For clinical datasets or third party data, please ensure that the statement adheres to our policy

Source data are provided with this paper. All data generated or analyzed during this study are included in the paper.

Research involving human participants, their data, or biological material

Policy information about studies with human participants or human data. See also policy information about sex, gender (identity/presentation), and sexual orientation and race, ethnicity and racism.

Reporting on sex and gender	None.
Reporting on race, ethnicity, or other socially relevant groupings	None.
Population characteristics	None.
Recruitment	None.
Ethics oversight	None.

Note that full information on the approval of the study protocol must also be provided in the manuscript.

Field-specific reporting

Please select the one below that is the best fit for your research. If you are not sure, read the appropriate sections before making your selection.

☐ Life sciences ☐ Behavioural & social sciences ☒ Ecological, evolutionary & environmental sciences

For a reference copy of the document with all sections, see nature.com/documents/nr-reporting-summary-flat.pdf

Ecological, evolutionary & environmental sciences study design

All studies must disclose on these points even when the disclosure is negative.

Study description	To investigate the effects of decomposition byproducts from robotic devices on plant growth, a comparative experiment was conducted to observe the growth patterns of oats in both regular soil and soil that has composted robotic devices.
Research sample	Pot A - control soil 100%, Pot B - 50% soil composted with robotic devices + 50% control soil, Pot C - 100% soil composted with robotic devices; 10 oat seeds were planted in each pot.
Sampling strategy	The height and weight of the plants are presented as mean values and standard deviations. The sample size is 10, and the experimental conditions are based on the ISO 11269-2 plant growth test.
Data collection	Kyung-Sub Kim collected the data. The height of the plants was measured with a ruler, and the weight was measured using an electronic scale.
Timing and spatial scale	The germination rate, survival rate, and height of the oat seeds were measured at intervals of 2-3 days. After 21 days of germination, the weight of the plants was analyzed.
Data exclusions	No data was excluded.
Reproducibility	None.
Randomization	None.
Blinding	None.

Did the study involve field work? ☐ Yes ☒ No

Reporting for specific materials, systems and methods

We require information from authors about some types of materials, experimental systems and methods used in many studies. Here, indicate whether each material, system or method listed is relevant to your study. If you are not sure if a list item applies to your research, read the appropriate section before selecting a response.

Materials & experimental systems

n/a | Involved in the study
- ☒ ☐ Antibodies
- ☒ ☐ Eukaryotic cell lines
- ☒ ☐ Palaeontology and archaeology
- ☒ ☐ Animals and other organisms
- ☒ ☐ Clinical data
- ☒ ☐ Dual use research of concern
- ☒ ☐ Plants

Methods

n/a | Involved in the study
- ☒ ☐ ChIP-seq
- ☒ ☐ Flow cytometry
- ☒ ☐ MRI-based neuroimaging

Plants

Seed stocks	None.
Novel plant genotypes	None.
Authentication	None.